NANO LETTERS

Letter

Cite This: *Nano Lett.* 2020, 20, 59−65

pubs.acs.org/NanoLett

Observation of Magnetic Antiskyrmions in the Low Magnetization Ferrimagnet $Mn_2Rh_{0.95}Ir_{0.05}Sn$

Jagannath Jena,[#] Rolf Stinshoff,[†] Rana Saha,[#] Abhay K. Srivastava,[#,§] Tianping Ma,[#] Hakan Deniz,[#] Peter Werner,[#] Claudia Felser,[†] and Stuart S. P. Parkin*[,#]

[#]Max Planck Institute of Microstructure Physics, Weinberg 2, 06120 Halle (Saale), Germany

[†]Max Planck Institute for Chemical Physics of Solids, Nöthnitzer Strasse 40, 01187 Dresden, Germany

[§]Institute of Physics, Martin Luther University, Halle-Wittenberg, 06120 Halle (Saale), Germany

S *Supporting Information*

ABSTRACT: Recently, magnetic antiskyrmions were discovered in $Mn_{1.4}Pt_{0.9}Pd_{0.1}Sn$, an inverse tetragonal Heusler compound that is nominally a ferrimagnet, but which can only be formed with substantial Mn vacancies. The vacancies reduce considerably the compensation of the moments between the two expected antiferromagnetically coupled Mn sub-lattices so that the overall magnetization is very high and the compound is almost a "ferromagnet". Here, we report the observation of antiskyrmions in a second inverse tetragonal Heusler compound, $Mn_2Rh_{0.95}Ir_{0.05}Sn$, which can be formed stoichiometrically without any Mn vacancies and which thus exhibits a much smaller magnetization. Individual and lattices of antiskyrmions can be stabilized over a wide range of temperature from near room temperature to 100 K, the base temperature of the Lorentz transmission electron microscope used to image them. In low magnetic fields helical spin textures are found which evolve into antiskyrmion structures in the presence of small magnetic fields. A weaker Dzyaloshinskii-Moriya interaction (DMI), that stabilizes the antiskyrmions, is expected for the 4d element Rh as compared to the 5d element Pt, so that the observation of antiskyrmions in $Mn_2Rh_{0.95}Ir_{0.05}Sn$ establishes the intrinsic stability of antiskyrmions in these Heusler compounds. Moreover, the finding of antiskyrmions with substantially lower magnetization promises, via chemical tuning, even zero moment antiskyrmions with important technological import.

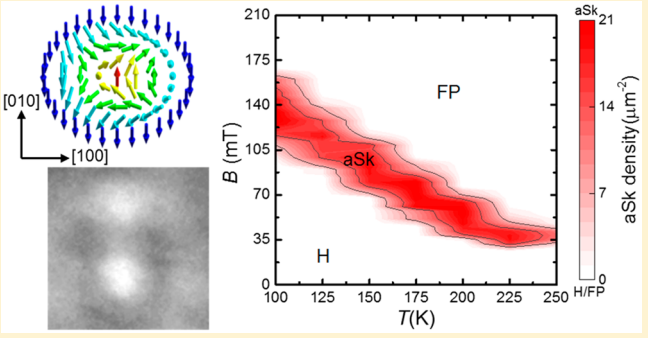

KEYWORDS: *Antiskyrmion, ferrimagnetic Heusler, low magnetic moment, Mn vacancies, Lorentz TEM, spintronics*

Magnetic skyrmions (Sks) are topologically protected vortices of magnetization that can be stabilized in magnetic materials with broken inversion symmetry.[1−9] Since the first observation of skyrmion lattices in the helimagnet MnSi,[4] a variety of noncollinear spin textures have been discovered in several distinct families of materials.[10−22] These spin textures have technological potential[23,24] as, for example, magnetic bits in high density storage devices such as racetrack memories[25−27] or for neuromorphic computing applications.[28] Recently, using Lorentz transmission electron microscopy (LTEM) a new topological spin texture that has distinct topological characteristics from that of Bloch and Néel skyrmions was discovered in a noncentrosymmetric inverse tetragonal Heusler compound. This compound with D_{2d} crystal symmetry stabilizes a novel noncollinear spin texture, namely an antiskyrmion (aSk).[29] However, the material in which the antiskyrmions were observed, $Mn_{1.4}Pt_{0.9}Pd_{0.1}Sn$, could only be stabilized by introducing a large number of Mn vacancies.[29] These vacancies strongly affect the overall magnetization of the compound.

The magnetic structure of Mn_2RhSn consists of two ferromagnetically aligned Mn sub-lattices that are antiferromagnetically coupled to each other[30] so leading to a net magnetic moment of ∼2 μ_B/f.u. at 2 K. By contrast, the magnetization of $Mn_{1.4}Pt_{0.9}Pd_{0.1}Sn$ and its close cousin $Mn_{1.4}PtSn$ is much higher, namely ∼4.5 μ_B/f.u. at 2 K.[29] Thus, it has been reported that $Mn_{1.4}Pt_{0.9}Pd_{0.1}Sn$ and $Mn_{1.4}PtSn$ are both effectively ferromagnets.[31−33] For spintronic devices, elimination of long-range dipole fields derived from the moments of small magnetic nano-objects is key to their success.[34−39] For application of antiskyrmions low or even zero moment hosting materials are very important. In this study we have explored the possibility of antiskyrmions in $Mn_2Rh_{0.95}Ir_{0.05}Sn$, a Heusler compound that has a significantly reduced magnetization compared to the only previous Heusler material in which antiskyrmions were observed, but with enough magnetization that the antiskyrmions can be observed

Received: July 20, 2019
Revised: December 4, 2019
Published: December 6, 2019

DOI: 10.1021/acs.nanolett.9b02973
Nano Lett. 2020, 20, 59−65

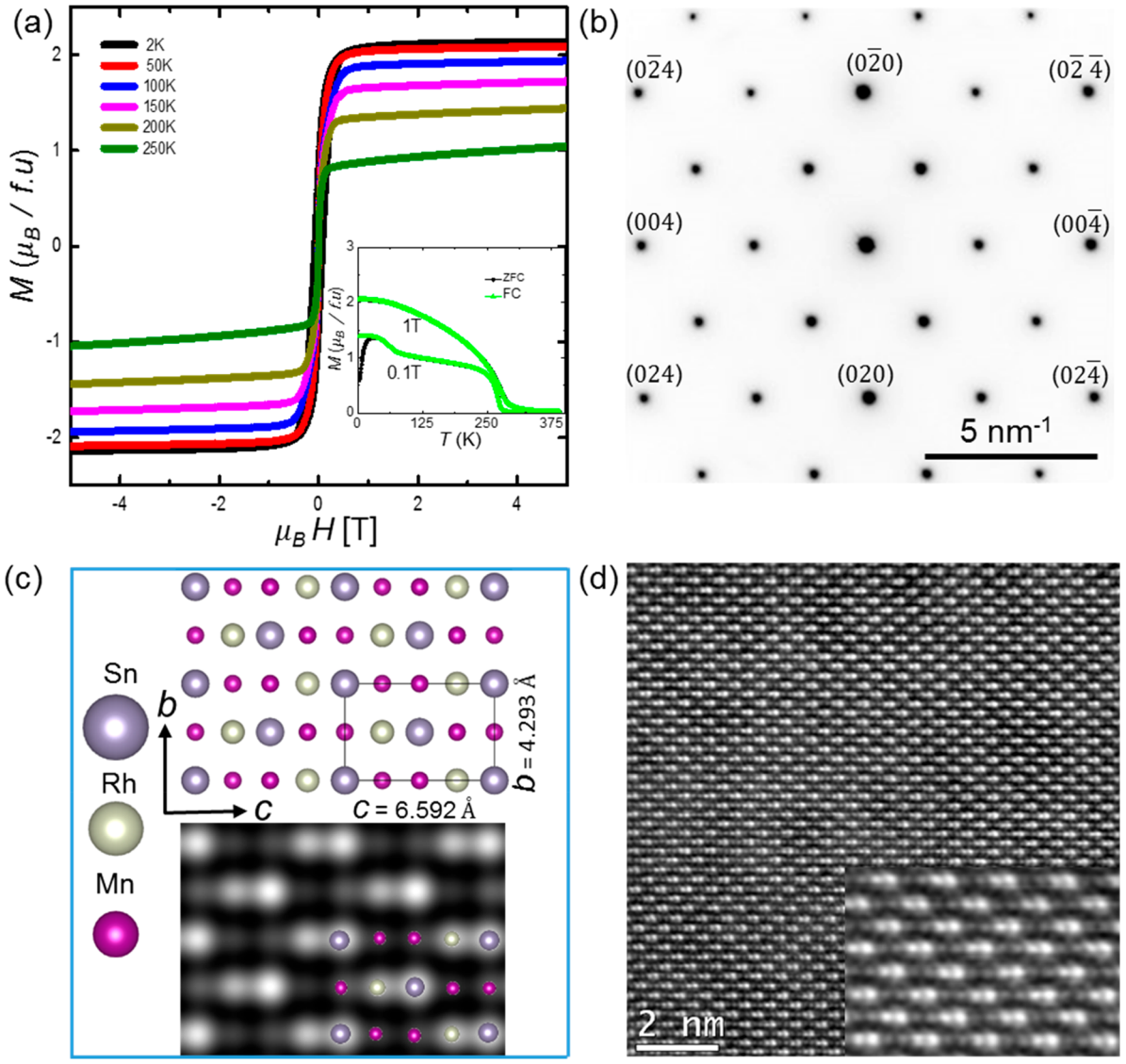

Figure 1. (a) $M(H)$ hysteresis loops at various temperatures. The inset displays ZFC (black color) and FC (green color) temperature dependent magnetization data in the presence of 0.1 T and 1 T fields. (b) Selected area electron diffraction (SAED) pattern from a thin lamella showing the [100] orientation. (c) The upper panel shows the schematic arrangement of Mn, Rh, and Sn atoms, and the lower panel shows a simulated STEM pattern with superimposed Mn, Rh, and Sn atoms as a guide to the eye. (d) Experimental STEM image along [100]: the inset shows an expanded view.

with Lorentz transmission electron microscopy. $Mn_2Rh_{0.95}Ir_{0.05}Sn$ can be formed without any significant Mn vacancies. We directly show the formation of antiskyrmions in this compound. This opens the path to the full exploitation of the considerable tunability of Heusler compounds for zero-moment antiskyrmions.

Polycrystalline samples of $Mn_2Rh_{0.95}Ir_{0.05}Sn$ were prepared by inductive melting of stoichiometric amounts of the elements Mn, Ir, Rh, and Sn of purity >99.99% in alumina crucibles. Due to the high melting points of iridium and rhodium, Rh and Ir powders were first prealloyed together with Sn. The alloy was kept in the melted state for approximately a minute before cooling down. This step was repeated three times to ensure good homogenization of the prealloy. Next, Mn chips were added to the Rh/Ir−Sn ingot followed by remelting and turning the ingots several times for better homogeneity. This procedure ensures a low loss of Mn due to evaporation, indeed for the final ingot, the total mass loss was below 0.5 wt % so that the composition of the ingot is close to the desired stoichiometry. The as-prepared ingots were then packed in closed tantalum crucibles that were further encapsulated in an evacuated fused quartz glass ampule. A subsequent heat treatment for 1 week at 900 °C was performed followed by quenching in an ice−water mixture resulting in the final polycrystalline ingot.

Polycrystalline samples were characterized by powder X-ray diffraction (PXRD) using an image-plate Guinier camera (Huber G670, Cu Kα_1, λ = 1.54059 Å). Peak search, indexing, and calculation of the diffraction patterns were performed with the aid of the WinXPow package.[40] All Bragg reflections can be indexed to a body-centered tetragonal unit cell with a = 4.293 (3) Å and c = 6.592 (4) Å. Rietveld refinement was carried out using the Jana2006 software.[41] The crystal structure was resolved by analogy with Mn_2RhSn, which crystallizes in the $I\bar{4}m2$ (D_{2d}) space group.[30] Under this symmetry Mn atoms occupy two different Wyckoff positions, namely MnI at 2b and

DOI: 10.1021/acs.nanolett.9b02973
Nano Lett. 2020, 20, 59−65

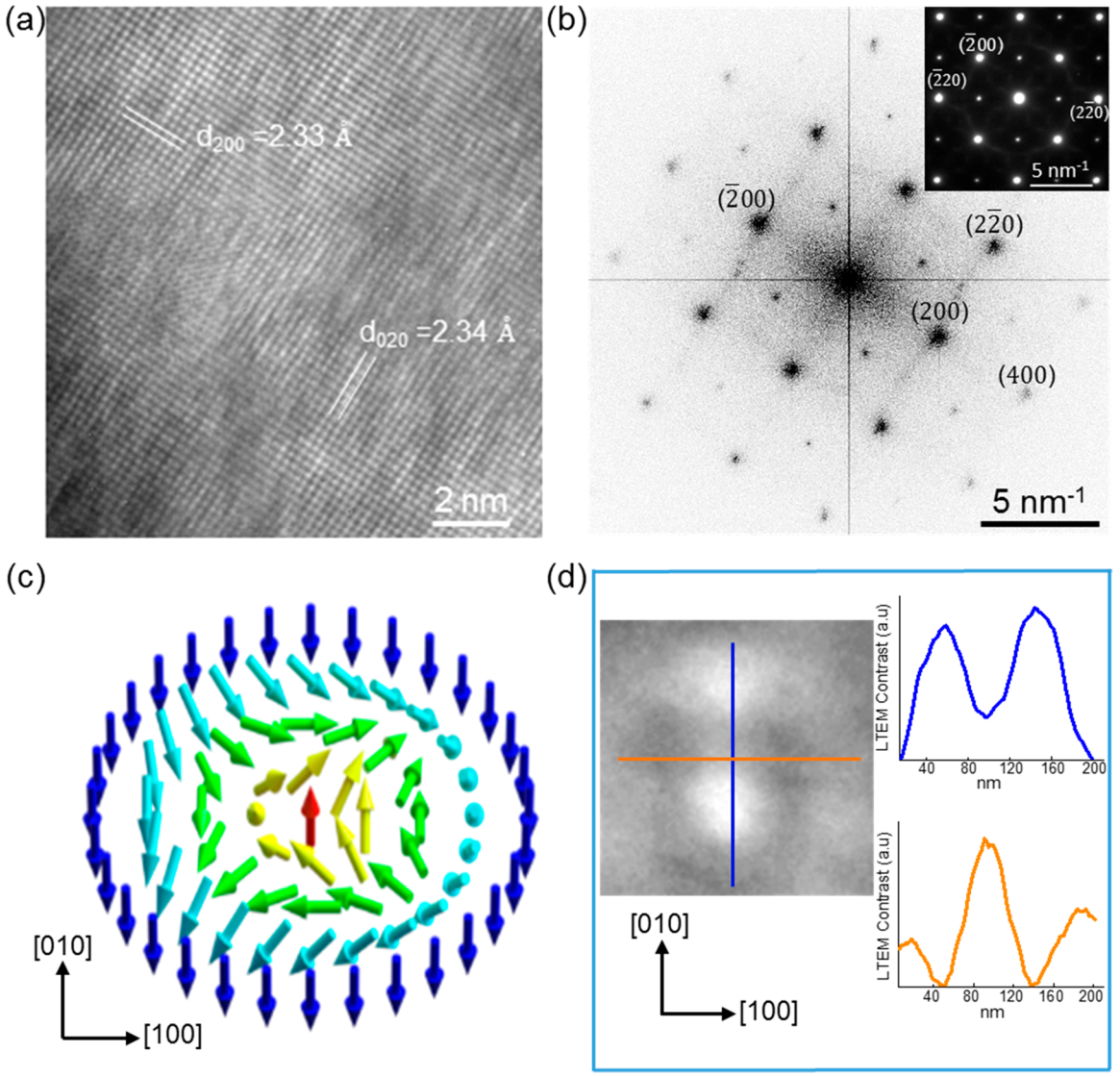

Figure 2. (a) High resolution transmission electron microscope image for a [001] oriented lamella and (b) the corresponding fast Fourier transform. The inset of Figure 1b shows the [001] oriented selected area electron diffraction (SAED) pattern. (c) Schematic of an antiskyrmion spin texture. (d) LTEM image of a single antiskyrmion at 150 K in the presence of a magnetic field of 83 mT. Inset shows the intensity profile of the contrast along [010] (blue color) and [100] (orange color) directions.

MnII at 2c, while Rh occupies 2d and Sn in the 2a position, respectively. For our refinement Ir was assumed to occupy the Rh position. Cases in which Ir additionally occupies the Sn or Mn sites do not lead to an improvement of the refinement, hence the later possibility is discarded. The Rietveld refinement of the XRD pattern is given in the Supporting Information (SI) (Figure S1). The stoichiometry of the titled compound from inductively coupled plasma optical emission spectrometry (ICP-OES) analysis is found to be $Mn_{1.988}Rh_{0.949}Ir_{0.049}Sn_{1.015}$ (within estimated standard deviation of 0.1−0.2 at %). In addition, the composition of the sample was also determined from energy-dispersive X-ray spectroscopy (EDXS) analysis that shows that it is stoichiometric (Figure S2).

The temperature and field (H) dependent DC magnetization (M) measurements of the bulk polycrystalline sample were carried out with a SQUID-VSM [MPMS3, Quantum design]. $M(H)$ loops measured at different temperatures are shown in Figure 1a. The saturation magnetization of this material is calculated from these measurements to be ∼2 μ_B/f.u. at 2 K and is reduced further to ∼1 μ_B/f.u. at 250 K. The saturation magnetization is nearly two times smaller than that of the first inverse Heusler material in which antiskyrmions were observed.[29] From the isothermal magnetization data it is apparent that this material is magnetically soft. The temperature dependent magnetization was measured in a field of 0.1 T for the temperature range from 2 to 390 K after both zero-field-cooling (ZFC) and field-cooling (FC) (Figure 1a). These data shows that the material undergoes a magnetic ordering transition from a paramagnetic to a ferrimagnetic state at ∼270 K with a second magnetic transition at 80 K. The latter transition has been attributed to a spin-canting transition that results from a competition between exchange interactions between Mn moments on neighboring and next nearest planes.[30] The spin-canting transition is suppressed in higher fields as seen from the temperature-dependent magnetization data at 1 T (see the inset of Figure 1a).

DOI: 10.1021/acs.nanolett.9b02973
Nano Lett. 2020, 20, 59−65

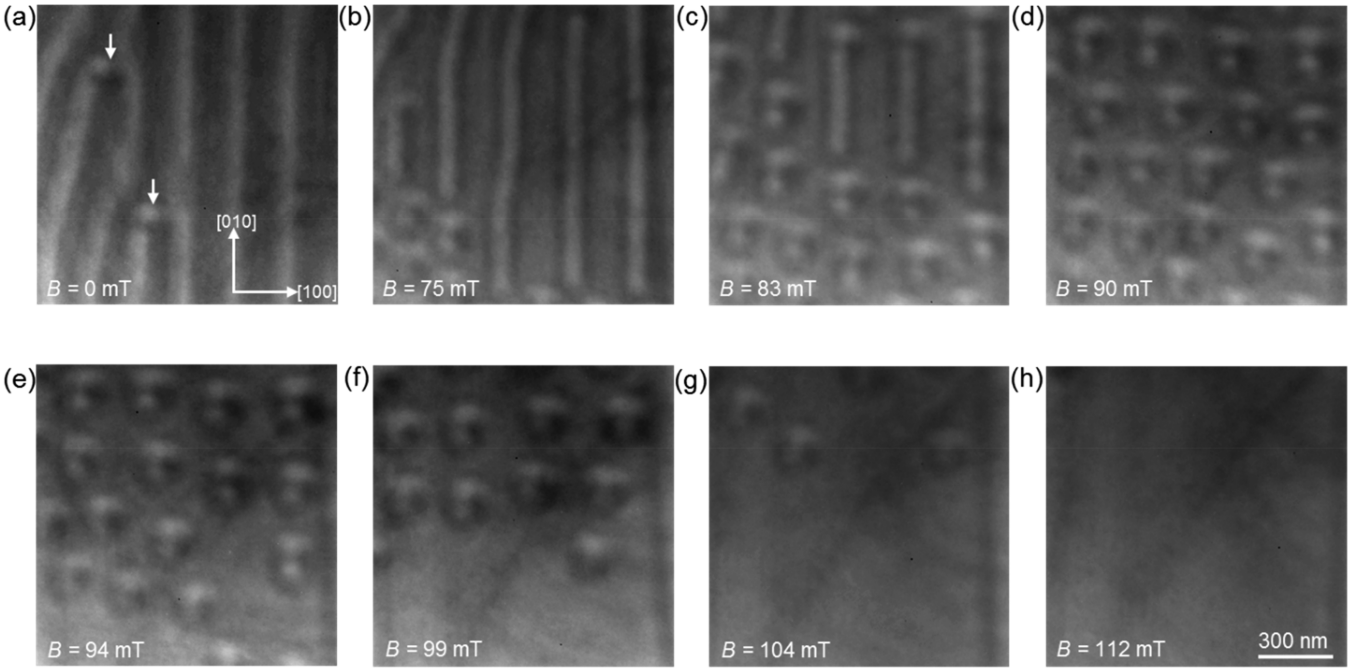

Figure 3. Lorentz transmission electron microscopy images of magnetic spin-textures at (a) zero magnetic field and (b–h) various magnetic fields at 150 K. Scale bar for all figures is identical and is given in (h).

For in-situ transmission electron microscopy (TEM) investigations, using a FEI TITAN 300 keV microscope, single crystalline lamellae, oriented along different crystal directions, were prepared from individual grains from within the polycrystalline $Mn_2Rh_{0.95}Ir_{0.05}Sn$ bulk sample. The small grain size (~10 μm) meant that this was nontrivial (Figure S3). The lamellae were prepared using a Ga-focused ion beam (FIB) milling at an acceleration voltage of 30 keV [FEI, Nova nano Lab]. Final polishing was carried out on both sides of the lamella using a low energy beam (2 keV) to reduce surface amorphization. In this way a [100] oriented lamella, approximately 60 nm thick, was prepared, as confirmed by the exemplary selected area electron diffraction pattern (SAED) shown in Figure 1b. A schematic atomic arrangement of the Sn, Rh, and Mn atomic columns along this zone axis is shown in Figure 1c. The schematic unit cell for this tetragonal structure is shown in the upper panel. In the lower panel, a simulated scanning transmission electron microscopy (STEM) image using the aforementioned space group is shown.[42] This simulated image is in agreement with the experimental STEM image given in Figure 1d. An enlarged portion of the image from the experimental STEM is shown in the inset of Figure 1d.

For crystals with D_{2d} symmetry,[29,30] an aSk lattice is stabilized within the tetragonal basal plane, so that it is necessary to carry out measurements on lamellae oriented along [001] in order to observe any aSk. High resolution TEM (HRTEM) images of such a lamella obtained in TEM mode are shown in Figure 2 showing (020) and (200) lattice planes. A fast Fourier transform (FFT) is given in Figure 2b together with the SAED (inset): these show that the lamella was [001] oriented.

To explore magnetic textures within the lamellae, Lorentz TEM (LTEM) was carried out using a GATAN double tilt liquid nitrogen sample holder that allows for variable temperatures between 100 K and room temperature. Clear evidence for the presence of aSk in the sample was found. A typical LTEM image of a single aSk at 150 K and 83 mT is shown in Figure 2d. This image is consistent with the schematic aSk spin structure shown in Figure 2c in which Bloch domain walls of opposite chirality are formed along the [100] and [010] directions, while Néel domain walls of opposite chirality are formed along the [110] and [1−10] directions. The inset of Figure 2d shows the LTEM contrast profile along the [010] and [100], respectively.

The magnetic field driven evolution of the aSk spin textures at a constant temperature (150 K) is examined after cooling the sample in zero magnetic field from 300 K. After stabilizing the temperature at 150 K, the LTEM images were recorded in zero field. These images show patterns in the form of alternating dark and light stripes, as shown in Figure 3a, which are characteristic of a helical spin structure. The direction of propagation of the helix is oriented along either [010] or [100] which are the directions along which Bloch domain walls are formed. The presence of magnetic dislocations is observed as the branching of helix marked by arrows in Figure 3a.[5,43,44] The movement and annihilation of these dislocations are observed upon application of a magnetic field (Figure S4). To apply a magnetic field to the sample, the sample was first tilted away from the [001] direction by ~25°, and a magnetic field was applied along the microscope column by adjusting the current in the objective lens. The sample was tilted back to a near zero degree tilt to record the LTEM images. This process of tilting, which allows for the application of a small in-plane magnetic field at the sample, was successively repeated to allow for LTEM images to be recorded at various perpendicular magnetic fields (zero degree tilt). This tilting procedure is needed to stabilize the aSk lattice.[29] Upon increasing the magnetic field following the aforementioned protocol, aSks were found to start to emerge from the helical spin texture at a field of ~75 mT and to coexist with the helical spin texture for fields up to ~83 mT

DOI: 10.1021/acs.nanolett.9b02973
Nano Lett. 2020, 20, 59–65

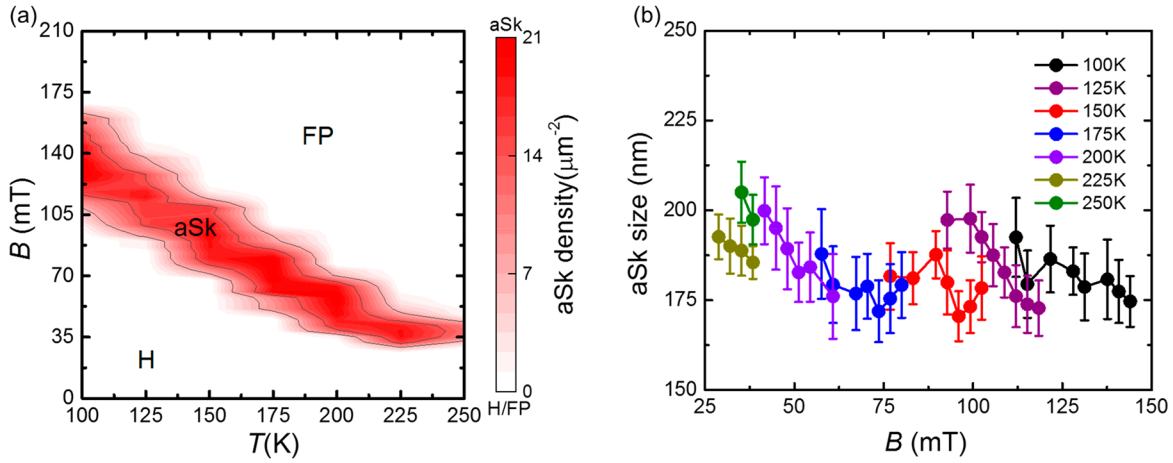

Figure 4. (a) Magnetic phase diagram of $Mn_2Rh_{0.95}Ir_{0.05}Sn$. (b) Antiskyrmion size as a function of perpendicular magnetic field at various temperatures. The error bars correspond to standard deviation in the aSk size. Here aSk, H, and FP correspond to antiskyrmion, helical, and field polarized states, respectively.

(Figure 3b,c). Further increments of the magnetic field (90−94 mT) lead to the formation of a pure aSk lattice, as shown in Figure 3d,e, which is a slightly distorted hexagonal array. We note that a well-defined strong hexagonal lattice is not found: the likely reason is the low moment of the antiskyrmions here which leads to weak magnetostatic interactions between them. With increasing the magnetic field up to ∼99−104 mT the density of aSks decreases (Figure 3f−g) and finally transforms to a fully field-polarized state at ∼112 mT (Figure 3h).

The evolution of the aSk texture as a function of magnetic field was performed at several temperatures. The results are summarized in the form of a magnetic phase diagram in Figure 4a. This phase diagram was constructed by cooling the sample from 300 to 100 K in zero magnetic field. After stabilizing the temperature at 100 K, the evolution of the helical to aSk lattice was studied using the protocol described in the previous paragraph. The temperature was subsequently increased successively in 25 K steps, and LTEM studies were carried out at each temperature. These results are presented in the magnetic phase diagram shown as a contour map of the aSk density in the temperature (T) - magnetic field (B) plane (Figure 4a). In the absence of magnetic field the ground state is the helical state. The period of the helix (λ) is in the range of ∼200−235 nm depending on the temperature (Figure S5). This period is larger by ∼50% than that reported for $Mn_{1.4}Pt_{0.9}Pd_{0.1}Sn$ for the same thickness of the LTEM sample. As λ is inversely proportional to DMI[12,45] the larger helical period in $Mn_2Rh_{0.95}Ir_{0.05}Sn$ is consistent with a weaker value of the DMI that is expected for the 4d element Rh as compared to the 5d element Pt.[46−48] From Figure 4a, it is clear that the generation of the aSk lattice from the helical phase requires lower magnetic fields at higher temperature or vice versa. The aSk lattice is stabilized over a wide window of temperature but in a relatively narrow magnetic field range. In Figure 4b the effect of magnetic field on the aSk size at different temperatures is shown. The aSk size was found using procedures discussed in reference 49. From this figure, we observe that at each temperature, there is a minute change in the size of aSks with field.

In conclusion, we have successfully identified the existence of magnetic aSks in an inverse ferrimagnetic Heusler compound, $Mn_2Rh_{0.95}Ir_{0.05}Sn$, that is fully stoichiometric, as compared with our earlier observations of aSks in the compound, $Mn_{1.4}Pt_{0.9}Pd_{0.1}Sn$, that contains substantial Mn vacancies and which, as a consequence, is nearly ferromagnetic. Antiskyrmions, in this second compound, are observed in a narrower region of field but, nevertheless, over a wide range of temperature. These results prove the intrinsic stability of a ground state composed of arrays of antiskyrmion in compounds that have D_{2d} symmetry and, moreover, show that antiskyrmions can be found in materials with low saturation magnetization as well as smaller DMI. Our work opens the path to the observation of antiskyrmions in the large number of materials that have D_{2d} symmetry, allowing for optimizing the properties of the host compounds, especially tuning the magnetization to zero, that would make them highly useful for various technological applications.

■ ASSOCIATED CONTENT

Supporting Information

The Supporting Information is available free of charge at https://pubs.acs.org/doi/10.1021/acs.nanolett.9b02973.

Figure S1, powder X-ray diffraction; Figure S2, scanning electron microscope (SEM) image and EDXS analyses; Figure S3, bright field, polarized light image, and EBSD; Figure S4, magnetic dislocations; Figure S5, comparison of helix period for $Mn_2Rh_{0.95}Ir_{0.05}Sn$ and $Mn_{1.4}Pt_{0.9}Pd_{0.1}Sn$; and Table S1, concentration of Mn, Rh, Ir, and Sn (PDF)

■ AUTHOR INFORMATION

Corresponding Author

*E-mail: stuart.parkin@mpi-halle.mpg.de.

ORCID

Stuart S. P. Parkin: 0000-0003-4702-6139

Author Contributions

J.J. performed LTEM and analyzed the data. J.J. and A.K.S. prepared the FIB lamellae. Magnetization measurements were carried out by Rolf S., J.J., and R.S. Rolf S. synthesized and characterized the samples. H.D., J.J., and P.W. performed the TEM measurements. J.J., R.S., and S.S.P.P. wrote the manuscript. All authors have discussed the results.

Notes

The authors declare no competing financial interest.

DOI: 10.1021/acs.nanolett.9b02973
Nano Lett. 2020, 20, 59−65

■ ACKNOWLEDGMENTS

The authors would like to acknowledge funding from the European Research Council (ERC) under the European Union's Horizon 2020 research and innovation programme (grant agreement SORBET No. 670166). We also thank the Deutsche Forschungs Gemeinschaft (DFG, German Research Foundation) − Project number 403505322.

■ REFERENCES

(1) Bogdanov, A.; Rößler, U.; Wolf, M.; Müller, K.-H. Magnetic structures and reorientation transitions in noncentrosymmetric uniaxial antiferromagnets. *Phys. Rev. B: Condens. Matter Mater. Phys.* **2002**, *66*, 214410.

(2) Bogdanov, A.; Hubert, A. Thermodynamically stable magnetic vortex states in magnetic crystals. *J. Magn. Magn. Mater.* **1994**, *138*, 255−269.

(3) Nagaosa, N.; Tokura, Y. Topological properties and dynamics of magnetic skyrmions. *Nat. Nanotechnol.* **2013**, *8*, 899.

(4) Mühlbauer, S.; Binz, B.; Jonietz, F.; Pfleiderer, C.; Rosch, A.; Neubauer, A.; Georgii, R.; Böni, P. Skyrmion lattice in a chiral magnet. *Science* **2009**, *323*, 915−919.

(5) Yu, X.; Onose, Y.; Kanazawa, N.; Park, J.; Han, J.; Matsui, Y.; Nagaosa, N.; Tokura, Y. Real-space observation of a two-dimensional skyrmion crystal. *Nature* **2010**, *465*, 901.

(6) Yu, X.; Kanazawa, N.; Onose, Y.; Kimoto, K.; Zhang, W.; Ishiwata, S.; Matsui, Y.; Tokura, Y. Near room-temperature formation of a skyrmion crystal in thin-films of the helimagnet FeGe. *Nat. Mater.* **2011**, *10*, 106.

(7) Moreau-Luchaire, C.; Moutafis, C.; Reyren, N.; Sampaio, J.; Vaz, C. a. F.; Van Horne, N.; Bouzehouane, K.; Garcia, K.; Deranlot, C.; Warnicke, P.; Wohlhüter, P.; George, J. M.; Weigand, M.; Raabe, J.; Cros, V.; Fert, A. Additive interfacial chiral interaction in multilayers for stabilization of small individual skyrmions at room temperature. *Nat. Nanotechnol.* **2016**, *11*, 444.

(8) Soumyanarayanan, A.; Raju, M.; Gonzalez Oyarce, A. L.; Tan, A. K. C.; Im, M.-Y.; Petrović, A. P.; Ho, P.; Khoo, K. H.; Tran, M.; Gan, C. K.; Ernult, F.; Panagopoulos, C. Tunable room-temperature magnetic skyrmions in Ir/Fe/Co/Pt multilayers. *Nat. Mater.* **2017**, *16*, 898.

(9) Pollard, S. D.; Garlow, J. A.; Yu, J.; Wang, Z.; Zhu, Y.; Yang, H. Observation of stable Néel skyrmions in cobalt/palladium multilayers with Lorentz transmission electron microscopy. *Nat. Commun.* **2017**, *8*, 14761.

(10) Heinze, S.; Von Bergmann, K.; Menzel, M.; Brede, J.; Kubetzka, A.; Wiesendanger, R.; Bihlmayer, G.; Blügel, S. Spontaneous atomic-scale magnetic skyrmion lattice in two dimensions. *Nat. Phys.* **2011**, *7*, 713.

(11) Seki, S.; Yu, X.; Ishiwata, S.; Tokura, Y. Observation of skyrmions in a multiferroic material. *Science* **2012**, *336*, 198−201.

(12) Tokunaga, Y.; Yu, X.; White, J.; Rønnow, H. M.; Morikawa, D.; Taguchi, Y.; Tokura, Y. A new class of chiral materials hosting magnetic skyrmions beyond room temperature. *Nat. Commun.* **2015**, *6*, 7638.

(13) Kézsmárki, I.; Bordács, S.; Milde, P.; Neuber, E.; Eng, L. M.; White, J. S.; Rønnow, H. M.; Dewhurst, C. D.; Mochizuki, M.; Yanai, K.; Nakamura, H.; Ehlers, D.; Tsurkan, V.; Loidl, A. Néel-type skyrmion lattice with confined orientation in the polar magnetic semiconductor GaV_4S_8. *Nat. Mater.* **2015**, *14*, 1116.

(14) Loudon, J. C.; Twitchett-Harrison, A. C.; Cortés-Ortuño, D.; Birch, M. T.; Turnbull, L. A.; Štefančič, A.; Ogrin, F. Y.; Burgos-Parra, E. O.; Bukin, N.; Laurenson, A.; Popescu, H.; Beg, M.; Hovorka, O.; Fangohr, H.; Midgley, P. A.; Balakrishnan, G.; Hatton, P. D. Do Images of Biskyrmions Show Type-II Bubbles? *Adv. Mater.* **2019**, *31*, 1806598.

(15) Jiang, W.; Upadhyaya, P.; Zhang, W.; Yu, G.; Jungfleisch, M. B.; Fradin, F. Y.; Pearson, J. E.; Tserkovnyak, Y.; Wang, K. L.; Heinonen, O.; Te Velthuis, S. G. E.; Hoffmann, A. Blowing magnetic skyrmion bubbles. *Science* **2015**, *349*, 283−286.

(16) Phatak, C.; Heinonen, O.; De Graef, M.; Petford-Long, A. Nanoscale skyrmions in a nonchiral metallic multiferroic: Ni_2MnGa. *Nano Lett.* **2016**, *16*, 4141−4148.

(17) Zheng, F.; Li, H.; Wang, S.; Song, D.; Jin, C.; Wei, W.; Kovács, A.; Zang, J.; Tian, M.; Zhang, Y.; Du, H.; Dunin-Borkowski, R. E. Direct Imaging of a Zero-Field Target Skyrmion and Its Polarity Switch in a Chiral Magnetic Nanodisk. *Phys. Rev. Lett.* **2017**, *119*, 197205.

(18) Zheng, F.; Rybakov, F. N.; Borisov, A. B.; Song, D.; Wang, S.; Li, Z.-A.; Du, H.; Kiselev, N. S.; Caron, J.; Kovács, A.; Tian, M.; Zhang, Y.; Blügel, S.; Dunin-Borkowski, R. E. Experimental observation of chiral magnetic bobbers in B20-type FeGe. *Nat. Nanotechnol.* **2018**, *13*, 451−455.

(19) Qian, F.; Bannenberg, L. J.; Wilhelm, H.; Chaboussant, G.; Debeer-Schmitt, L. M.; Schmidt, M. P.; Aqeel, A.; Palstra, T. T. M.; Brück, E.; Lefering, A. J. E.; Pappas, C.; Mostovoy, M.; Leonov, A. O. New magnetic phase of the chiral skyrmion material Cu_2OSeO_3. *Sci. Adv.* **2018**, *4*, No. eaat7323.

(20) Caretta, L.; Mann, M.; Büttner, F.; Ueda, K.; Pfau, B.; Günther, C. M.; Hessing, P.; Churikova, A.; Klose, C.; Schneider, M.; Engel, D.; Marcus, C.; Bono, D.; Bagschik, K.; Eisebitt, S.; Beach, G. S. D. Fast current-driven domain walls and small skyrmions in a compensated ferrimagnet. *Nat. Nanotechnol.* **2018**, *13*, 1154−1160.

(21) Yu, X.; Koshibae, W.; Tokunaga, Y.; Shibata, K.; Taguchi, Y.; Nagaosa, N.; Tokura, Y. Transformation between Meron and skyrmion topological spin textures in a chiral magnet. *Nature* **2018**, *564*, 95.

(22) Das, S.; Tang, Y. L.; Hong, Z.; Gonçalves, M. a. P.; Mccarter, M. R.; Klewe, C.; Nguyen, K. X.; Gómez-Ortiz, F.; Shafer, P.; Arenholz, E.; Stoica, V. A.; Hsu, S. L.; Wang, B.; Ophus, C.; Liu, J. F.; Nelson, C. T.; Saremi, S.; Prasad, B.; Mei, A. B.; Schlom, D. G.; Íñiguez, J.; García-Fernández, P.; Muller, D. A.; Chen, L. Q.; Junquera, J.; Martin, L. W.; Ramesh, R. Observation of room-temperature polar skyrmions. *Nature* **2019**, *568*, 368−372.

(23) Jonietz, F.; Mühlbauer, S.; Pfleiderer, C.; Neubauer, A.; Münzer, W.; Bauer, A.; Adams, T.; Georgii, R.; Böni, P.; Duine, R. A.; Everschor, K.; Garst, M.; Rosch, A. Spin Transfer Torques in MnSi at Ultralow Current Densities. *Science* **2010**, *330*, 1648−1651.

(24) Yu, X.; Kanazawa, N.; Zhang, W.; Nagai, T.; Hara, T.; Kimoto, K.; Matsui, Y.; Onose, Y.; Tokura, Y. Skyrmion flow near room temperature in an ultralow current density. *Nat. Commun.* **2012**, *3*, 988.

(25) Tomasello, R.; Martinez, E.; Zivieri, R.; Torres, L.; Carpentieri, M.; Finocchio, G. A strategy for the design of skyrmion racetrack memories. *Sci. Rep.* **2015**, *4*, 6784.

(26) Parkin, S. S.; Hayashi, M.; Thomas, L. Magnetic domain-wall racetrack memory. *Science* **2008**, *320*, 190−194.

(27) Fert, A.; Cros, V.; Sampaio, J. Skyrmions on the track. *Nat. Nanotechnol.* **2013**, *8*, 152.

(28) Li, S.; Kang, W.; Huang, Y.; Zhang, X.; Zhou, Y.; Zhao, W. Magnetic skyrmion-based artificial neuron device. *Nanotechnology* **2017**, *28*, 31LT01.

(29) Nayak, A. K.; Kumar, V.; Ma, T.; Werner, P.; Pippel, E.; Sahoo, R.; Damay, F.; Rößler, U. K.; Felser, C.; Parkin, S. S. Magnetic antiskyrmions above room temperature in tetragonal Heusler materials. *Nature* **2017**, *548*, 561.

(30) Meshcheriakova, O.; Chadov, S.; Nayak, A. K.; Rößler, U. K.; Kübler, J.; André, G.; Tsirlin, A. A.; Kiss, J.; Hausdorf, S.; Kalache, A.; Schnelle, W.; Nicklas, M.; Felser, C. Large Noncollinearity and Spin Reorientation in the Novel Mn_2RhSn Heusler Magnet. *Phys. Rev. Lett.* **2014**, *113*, 087203.

(31) Vir, P.; Gayles, J.; Sukhanov, A.; Kumar, N.; Damay, F.; Sun, Y.; Kübler, J.; Shekhar, C.; Felser, C. Anisotropic topological Hall effect with real and momentum space Berry curvature in the antiskyrmion-hosting Heusler compound $Mn_{1.4}PtSn$. *Phys. Rev. B: Condens. Matter Mater. Phys.* **2019**, *99*, 140406.

(32) Vir, P.; Kumar, N.; Borrmann, H.; Jamijansuren, B.; Kreiner, G.; Shekhar, C.; Felser, C. Tetragonal superstructure of the

DOI: 10.1021/acs.nanolett.9b02973
Nano Lett. 2020, 20, 59−65

antiskyrmion hosting Heusler compound $Mn_{1.4}PtSn$. *Chem. Mater.* **2019**, *31*, 5876−5880.
(33) Kumar, V.; Kumar, N.; Reehuis, M.; Gayles, J.; Sukhanov, A. S.; Hoser, A.; Damay, F.; Sekhar, C.; Adler, P.; Felser, C. Detection of antiskyrmions by topological Hall effect in Heusler compounds. *Phys. Rev. B* 2019, in press.
(34) Jungwirth, T.; Marti, X.; Wadley, P.; Wunderlich, J. Antiferromagnetic spintronics. *Nat. Nanotechnol.* **2016**, *11*, 231.
(35) Baltz, V.; Manchon, A.; Tsoi, M.; Moriyama, T.; Ono, T.; Tserkovnyak, Y. Antiferromagnetic spintronics. *Rev. Mod. Phys.* **2018**, *90*, 015005.
(36) Duine, R.; Lee, K.-J.; Parkin, S. S.; Stiles, M. D. Synthetic antiferromagnetic spintronics. *Nat. Phys.* **2018**, *14*, 217.
(37) Gomonay, O.; Baltz, V.; Brataas, A.; Tserkovnyak, Y. Antiferromagnetic spin textures and dynamics. *Nat. Phys.* **2018**, *14*, 213.
(38) Zhang, X.; Zhou, Y.; Ezawa, M. Antiferromagnetic skyrmion: stability, creation and manipulation. *Sci. Rep.* **2016**, *6*, 24795.
(39) Yang, S.-H.; Ryu, K.-S.; Parkin, S. Domain-wall velocities of up to 750 m s- 1 driven by exchange-coupling torque in synthetic antiferromagnets. *Nat. Nanotechnol.* **2015**, *10*, 221.
(40) *Software WinXPow*; Stoe & Cie GmbH: Darmstadt, Germany, 2011; Vol. *298*.
(41) Petricek, V.; Dusek, M.; Palatinus, L. *Jana2006*; Structure determination software programs; Institute of Physics, University of Prague: Prague, Czech Republic, 2006.
(42) Ishizuka, K. A practical approach for STEM image simulation based on the FFT multislice method. *Ultramicroscopy* **2002**, *90*, 71−83.
(43) Uchida, M.; Onose, Y.; Matsui, Y.; Tokura, Y. Real-space observation of helical spin order. *Science* **2006**, *311*, 359−361.
(44) Dussaux, A.; Schoenherr, P.; Koumpouras, K.; Chico, J.; Chang, K.; Lorenzelli, L.; Kanazawa, N.; Tokura, Y.; Garst, M.; Bergman, A.; Degen, C. L.; Meier, D. Local dynamics of topological magnetic defects in the itinerant helimagnet FeGe. *Nat. Commun.* **2016**, *7*, 12430.
(45) Kanazawa, N.; Seki, S.; Tokura, Y. Noncentrosymmetric magnets hosting magnetic skyrmions. *Adv. Mater.* **2017**, *29*, 1603227.
(46) Jia, H.; Zimmermann, B.; Blügel, S. First-principles investigation of chiral magnetic properties in multilayers: Rh/Co/Pt and Pd/Co/Pt. *Phys. Rev. B: Condens. Matter Mater. Phys.* **2018**, *98*, 144427.
(47) Hellman, F.; Hoffmann, A.; Tserkovnyak, Y.; Beach, G. S.; Fullerton, E. E.; Leighton, C.; Macdonald, A. H.; Ralph, D. C.; Arena, D. A.; Dürr, H. A. Interface-induced phenomena in magnetism. *Rev. Mod. Phys.* **2017**, *89*, 025006.
(48) Ryu, K.-S.; Yang, S.-H.; Thomas, L.; Parkin, S. S. Chiral spin torque arising from proximity-induced magnetization. *Nat. Commun.* **2014**, *5*, 3910.
(49) Saha, R.; Srivastava, A. K.; Ma, T.; Jena, J.; Werner, P.; Kumar, V.; Felser, C.; Parkin, S. S. Intrinsic stability of magnetic anti-skyrmions in the tetragonal inverse Heusler compound $Mn_{1.4}Pt_{0.9}Pd_{0.1}Sn$. *Nat. Commun.* **2019**, *10*, 5305.

DOI: 10.1021/acs.nanolett.9b02973
Nano Lett. 2020, 20, 59−65